ACS APPLIED MATERIALS & INTERFACES

Research Article

www.acsami.org

Mg-Doped ZnO Nanoparticles for Efficient Sunlight-Driven Photocatalysis

Vinodkumar Etacheri,[†] Roshith Roshan,[‡] and Vishwanathan Kumar*[,‡]

[†]Department of Chemistry, Bar-Ilan University, Ramat Gan 52900, Israel

[‡]Centre for Materials for Electronics Technology, Scientific Society, Department of Information Technology, Ministry of Communications and Information Technology, Government of India, Shornur Road, M.G.Kavu, Athani P.O., Trissur 680 771, Kerala, India

Supporting Information

ABSTRACT: Magnesium-doped ZnO (ZMO) nanoparticles were synthesized through an oxalate coprecipitation method. Crystallization of ZMO upon thermal decomposition of the oxalate precursors was investigated using differential scanning calorimetry (DSC) and X-ray diffraction (XRD) techniques. XRD studies point toward a significant *c*-axis compression and reduced crystallite sizes for ZMO samples in contrast to undoped ZnO, which was further confirmed by HRSEM studies. X-ray photoelectron spectroscopy (XPS), UV/vis spectroscopy and photoluminescence (PL) spectroscopy were employed to establish the electronic and optical properties of these nanoparticles. (XPS) studies confirmed the substitution of Zn^{2+} by Mg^{2+}, crystallization of MgO secondary phase, and increased Zn−O bond strengths in Mg-doped ZnO samples. Textural properties of these ZMO samples obtained at various calcination temperatures were superior in comparison to the undoped ZnO. In addition to this, ZMO samples exhibited a blue-shift in the near band edge photoluminescence (PL) emission, decrease of PL intensities and superior sunlight-induced photocatalytic decomposition of methylene blue in contrast to undoped ZnO. The most active photocatalyst 0.1-MgZnO obtained after calcination at 600 °C showed a 2-fold increase in photocatalytic activity compared to the undoped ZnO. Band gap widening, superior textural properties and efficient electron−hole separation were identified as the factors responsible for the enhanced sunlight-driven photocatalytic activities of Mg-doped ZnO nanoparticles.

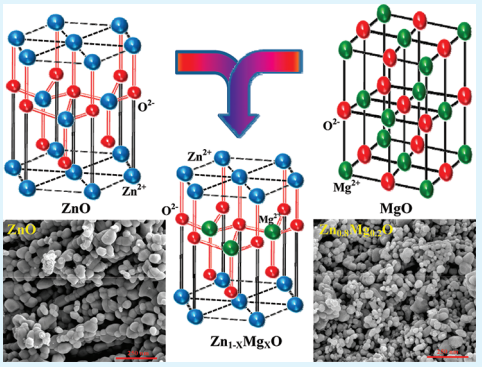

KEYWORDS: *zinc oxide, oxalate route, Mg doping, photocatalysis, methylene blue degradation*

1. INTRODUCTION

Significant advances have recently been made in the area of semiconductor nanostructures for photocatalytic applications.[1−5] High redox potential, large exciton binding energy (~60 meV), superior physical and chemical stability, inexpensiveness, and nontoxicity were identified as the main reasons responsible for the wide acceptability of ZnO materials compared to other semiconductor photocatalysts.[2,6−8] ZnO crystallizes in a hexagonal wurtzite structure (a = 3.25 Å, c = 5.20 Å), which possess a band gap of 3.37 eV and Hall mobility of the order of 200 $cm^2\ V^{-1}\ s^{-1}$ at room temperature.[9,10] Several researchers confirmed the fact that ZnO is preferred over TiO_2 for the photocatalytic decomposition of organic pollutants due to its high quantum efficiency.[11−14] In addition to this, ZnO can absorb and utilize larger fractions of solar spectrum compared to TiO_2.[15] Photocatalytic activity of ZnO depends on various factors such as phase purity, surface area, crystallite size, nature of dopants, and method of preparation.

Though ZnO is highly photocatalytically active, its band gap is not wide enough to utilize the high-energy solar radiations (UV−B and UV−C).[16] This narrow band gap seriously deteriorates the photocatalytic activities of ZnO under sunlight irradiation, which has significant impacts on the commercial applications of these materials. In order to utilize solar radiations more effectively, the development of a wide band gap ZnO is necessary.[16] Transition metal and anionic doping were employed previously for improving the photocatalytic activity of ZnO under sunlight irradiation.[17−19] Photocatalytic activities of these transition metal- and anion-doped ZnO were not sufficient for real-life applications because of an increase in charge carrier recombination centers. Dye sensitization was another technique employed for enhancing the photocatalytic activity, which has the serious drawback of dye decomposition during sunlight irradiation.[20] Under these circumstances, it is necessary to develop a highly sunlight-active ZnO photocatalyst.

One of the promising methods to widen the band gap is to synthesize a solid solution of ZnO and another semiconductor with a wider band gap such as MgO (band gap = 7.8 eV).[16,21−23] By varying the Mg-content, the band gap can be

Received: February 28, 2012
Accepted: May 3, 2012
Published: May 3, 2012

tuned from 3.3 to 7.8 eV for wurtzite and cubic structured $Mg_xZn_{1-x}O$.[21,22] This results in the extension of absorption wavelengths from UV-A (320−400 nm) to UV−B (280−320 nm) and UV−C (200−280 nm) regions.[21] Recently, a great deal of work has been reported on Mg-doped ZnO (ZMO), which possesses attractive properties for potential applications in novel optoelectronic and nanoelectronic devices.[24,25] In addition to this, wide band gap ZMO semiconductors have been found to be promising candidates for solar cells, gas sensors, liquid crystal displays, heat mirrors, solar UV-radiation monitoring, ultrahigh temperature flame detection and airborne missile warning systems.[26−29] ZMO is a solid solution consisting of ZnO and MgO, which has wurtzite hexagonal structure (a = 3.25 Å and c = 5.20 Å) and NaCl-type cubic structure (a = 4.24 Å), respectively.[30] ZMO alloys can exist as either hexagonal or cubic crystals due to structural dissimilarity between ZnO and MgO. Despite this lattice mismatch, the comparable ionic radii (Zn^{2+} = 0.60 Å and Mg^{2+} = 0.57 Å), serves as a possibility for the solid solution formation.[10] Various physical and chemical methods such as magnetron sputtering, pulsed laser deposition, sol−gel, spray pyrolysis and solution processing have been employed for the synthesis of wide band gap ZMO solid solution.[31−33] The phase diagram of Mg: ZnO predicts that the solubility of Mg only up to 4 at. % can be achieved in the ZnO wurtzite phase. This solubility limit of MgO in ZnO is widely varying and was found to be depending on the growth technique used. Though there are many reports on the electronic and photonic applications of the ZMO, little attention has been directed toward the sunlight-driven photocatalytic applications of this material. The work described herein describes the effect of Mg-doping on the photocatalytic activities of ZnO under sunlight irradiation. In this method, ZMO particles were synthesized through an oxalate coprecipitation method, and the band gap values were tuned by varying the Mg content. The effect of Mg doping on the crystal structure and physical properties of ZnO nanoparticles were systematically investigated using spectroscopic and microscopic techniques.

2. EXPERIMENTAL METHODS

2.1. Synthesis of Mg-Doped ZnO. The raw materials used for the preparation of Mg-doped ZnO included dry purified AR grade $ZnCl_2$, oxalic acid, $MgNO_3.6H_2O$ and concentrated HNO_3 (all from Merck chemicals). In the chemical route, the phase pure ZnO and $Zn_{1-x}Mg_xO$ powders with "x" ranging from 0.02, 0.05, 0.10, and 0.20 were prepared by the oxalate coprecipitation method. In order to prepare pure ZnO, a clear aqueous solution of $ZnCl_2$ was prepared by adding small amounts of concentrated HNO_3. This clear solution was then added to hot oxalic acid (~60 °C), and the pH of the solution was adjusted to 4.2 and stirred for 1 h. After cooling, the white precipitate formed was filtered, washed, and dried in an air oven at 100 °C for 12 h. The xerogel obtained was then calcined at various temperatures in the range 400−700 °C for 2 h at a heating rate of 10 °C/min. $Zn_{1-x}Mg_xO$ compositions within the above range was prepared similarly by adding a mixture of $ZnCl_2$ and $MgNO_3{\cdot}6H_2O$ in the required stoichiometric amounts into the hot oxalic acid solution maintaining the above procedure (identified as ZnO, 0.02-MgZnO, 0.05-MgZnO, 0.10-MgZnO, and 0.20-MgZnO after calcination).

2.2. Characterization Techniques. The FT-IR spectra of xerogel dried at 100 °C and calcined at various temperatures were recorded in the range of 4000−400 cm^{-1} using a Nicolet Magna-560 spectrometer. For recording the spectra, samples were uniformly mixed with KBr and transparent pellets were prepared by using a 4 mm die. Shimadzu DSC-60 and TA-Instruments SDT-Q600 instruments were used for differential scanning calorimetry (DSC) and thermo gravimetric analysis (TGA), respectively. In both cases, xerogel samples (5 mg) were heated from 30 to 600 °C at a constant heating rate of 10 °C/min. X-ray diffraction patterns (2θ = 10−70°) were obtained from a Rigaku Dmax-2500 diffractometer working with Cu−Kα radiation (λ = 0.15418 nm). Scherrer equation (eq 1) was employed for the precise calculation of the crystallite sizes of ZnO samples calcined at various temperatures.[34]

$$\Phi = \frac{K\lambda}{\beta\cos\theta} \tag{1}$$

Where Φ is the crystallite size, λ is the wavelength of X-ray used; K is the shape factor, β is the full line width at the half-maximum height of the main intensity peak, and θ is the Bragg angle. Lattice parameters a and c of the pure and Mg-doped ZnO samples were calculated from (100) and (002) oriented XRD peaks using eqs 2 and 3.[35]

$$a = \frac{\lambda}{\sqrt{3}\sin\theta} \tag{2}$$

$$c = \frac{\lambda}{\sin\theta} \tag{3}$$

The surface morphologies and size distribution of the ZnO samples were characterized using an ultra-high-resolution scanning electron microscope (HRSEM, Hitachi S4100). X-ray photoelectron spectra were recorded using a Kratos Axis HS spectrometer (England) equipped with an Al−Kα X-ray radiation source (photon energy 1486.6 eV). Charge compensation of the samples during the XPS analysis was achieved using a low-energy electron flood gun. The binding energies of various elements were calculated by fixing the CC/CH component of the C 1s peak at 285 eV. Optical absorption spectra of powder samples were obtained from a Shimadzu-2101 UV/vis spectrometer equipped with an integrated sphere attachment and $BaSO_4$ reference. The powder samples were thoroughly mixed with anhydrous KBr and discs were prepared by using a 4 mm die. The Kubelka-Munk function $F(R_\infty)$ was plotted against wavelength and band gaps were calculated by extrapolating the lower wavelength cutoff region. The nitrogen adsorption and desorption isotherms were collected using a Quantachrome-1000e surface area analyzer. Prior to the analysis, all samples were vacuum degassed at 300 °C for 2 h. The linear portion (P/P_o = 0.05−0.2) of the Brunauer−Emmett−Teller (BET) model was used for the calculation of specific surface area. Pore diameter and pore volumes were calculated from the desorption branch of the Barret-Joyner-Halenda (BJH) model. For analyzing the photoluminescence (PL) spectra, powder samples were dispersed in deionized water (0.01 g in 100 mL) with the help of an ultrasonicator (for 30 min) and spectra were recorded using a Perkin-Elmer PL spectrometer (LS-55B) at an excitation wavelength of 260 nm.

2.3. Photocatalysis Study. Sunlight-induced photocatalytic activities of Mg-doped ZnO samples were analyzed through methylene blue degradation technique using Q-Sun solar-simulator as the light source. In a typical photocatalytic degradation experiment, an aqueous solution of methylene blue (50 mL of 1×10^{-5} M) was mixed and stirred well with ZnO powder (0.06 g) in a glass beaker (100 mL). The suspension thus obtained was kept under dark for 30 min and then irradiated with simulated sunlight (0.68 W/m^2) with stirring. An air cooler and thermostat were connected to the solar simulator to maintain the temperature of suspension at 25 °C. Aliquots (3 mL) were withdrawn from the suspension under sunlight irradiation at equal time intervals, and the absorption spectra were recorded using a Shimadzu- 2101 UV/vis spectrometer. The photocatalytic rate constant for methylene blue degradation (k) was determined from the first-order plot using eq 4.

$$\ln\left(\frac{A_0}{A}\right) = kt \tag{4}$$

Where A_0 is the initial absorbance, A is the absorbance after a time t, and k is the first-order rate constant.

3. RESULTS AND DISCUSSION

3.1. Formation of $Zn_{1-x}Mg_xO$ Nanoparticles. The nature of reaction intermediates and formation of nanocrystalline ZnO wurtzite structure were investigated using FTIR spectroscopy (Figure 1). The spectrum of 100 °C dried oxalate

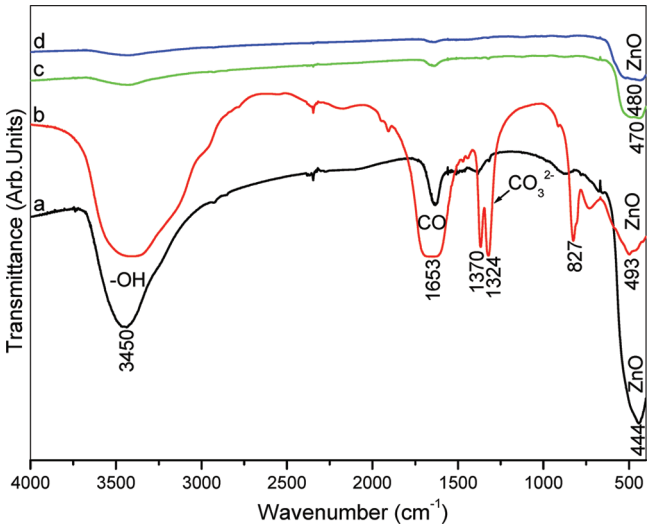

Figure 1. FTIR spectra of (a) ZnO as-prepared at 100 °C, (b) 0.20-MgZnO as prepared at 100 °C, (c) ZnO calcined at 400 °C, (d) 0.20-MgZnO calcined at 400 °C.

precursor of ZnO and MgZnO showed an absorption peak at 3450 cm^{-1}, which corresponds to the O−H stretching of surface adsorbed water molecule.[36,37] Peaks representing crystalline ZnO were identified in these 100 °C dried oxalate precursors of ZnO and MgZnO samples around 444 and 493 cm^{-1} respectively. Interestingly, the peaks characteristics of ZnC_2O_4 were not observed in the dried ZnO precursor, and the 1653 cm^{-1} peak can be ascribed to the presence of residual oxalic acid. This was because of the crystallization of ZnO at 100 °C, which will be proved using XRD and DSC studies in later stages of the discussion. On the other hand, the MgZnO oxalate precursor exists as $[Mg(C_2O_4).2H_2O]$, which was identified from the peaks at 827, 1324, 1370, and 1653 cm^{-1}.[38] However, after calcination at 400 °C, the peaks corresponding to organic precursors were no longer present, and only the peak corresponding to ZnO (Zn−O) was present. It should be noted that the Zn−O peaks for Mg doped ZnO appeared at higher wavenumbers in contrast to pure ZnO, before and after calcination. For example the Zn−O peak of ZnO and 0.20-MgZnO calcined at 400 °C appeared at 470 and 480 cm^{-1} respectively. This may be due to the incorporation of Mg^{2+} in to the ZnO crystal structure, which was later confirmed using the XRD and XPS techniques.

To investigate the thermal characteristics of ZnO and MgZnO oxalate precursors, we carried out differential scanning calorimetry (DSC) and thermogravimetric analysis (TGA) analysis. For all oxalate precursors, evaporation of adsorbed water molecules was observed as an endothermic DSC peak at 60 °C (Figure 2A). It should be noted that there are no distinct endothermic peaks characteristics of ZnC_2O_4 decomposition, which proved the fact that ZnO crystallization occurs during drying the ZnO precursor at 100 °C. The broad endothermic peak appeared in this case after 300 °C results from the evaporation of residual oxalic acid. The endothermic peaks observed around 170 °C for MgZnO oxalate precursor can be attributed to the removal of structural water present in $[Mg(C_2O_4)\cdot 2H_2O]$. An endothermic peak around 394 °C represents the decomposition of magnesium oxalate complex. An additional endothermic peak around 460 °C is characteristic of the decomposition of amorphous $Mg(OH)_2$ to form crystalline MgO, which was pronounced in the case of 0.20-MgZnO precursor. The TGA pattern of ZnO and MgZnO oxalate precursors are presented in Figure 2B. The total weight loss calculated for ZnO precursor on heat treatment was only 3%. In contrast, 0.02-MgZnO, 0.10-MgZnO and 0.20-MgZnO precursors experienced increased weight loss of 5.5, 12, and 46%, respectively. The weight loss of ZnO precursor happens in the range of 300−400 °C due to the evaporation of residual oxalic acid. On the other hand, MgZnO oxalate precursor decompose in two distinct temperature intervals (100−180 °C, and 350−470 °C) corresponding to the removal of structural water and decomposition of $[Mg(C_2O_4)\cdot 2H_2O]$ to MgO.

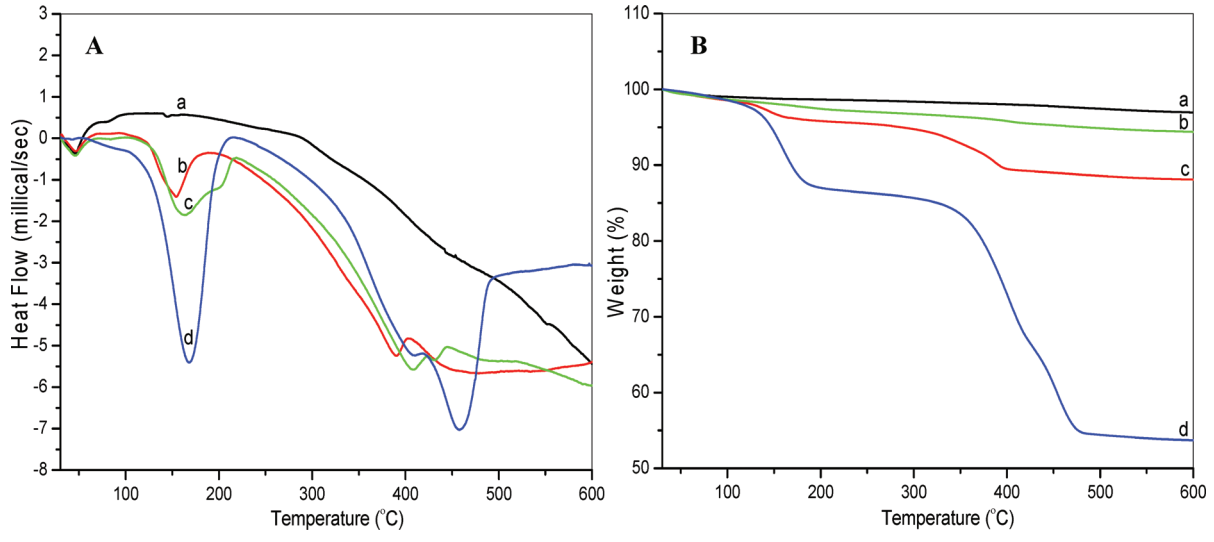

Figure 2. (A) Differential scanning calorimetric and (B) thermogravimetric pattern of (a) ZnO, (b) 0.02-MgZnO, (c) 0.10-MgZnO, (d) 0.20-MgZnO.

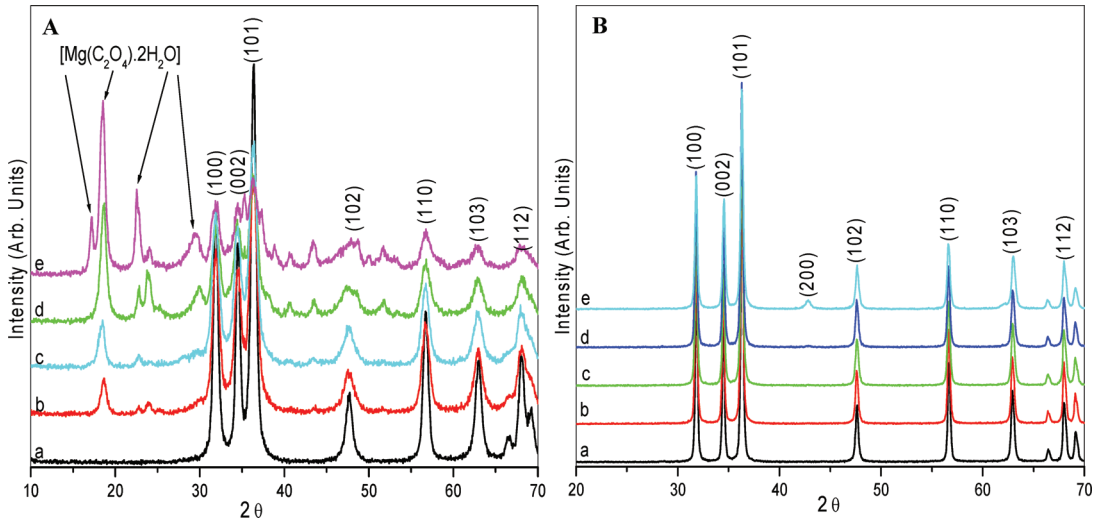

Figure 3. XRD of ZnO samples: (A) dried at 100 °C, (B) calcined at 500 °C: (a) ZnO, (b) 0.02-MgZnO, (c) 0.05-MgZnO, (d) 0.10-MgZnO, (e) 0.20-MgZnO.

Crystallization of ZnO and MgZnO nanostructures were identified from the XRD patterns recorded after calcination at various temperatures. XRD pattern of ZnO oxalate precursor dried AT 100 °C is presented in Figure 3A, which corresponds to phase pure wurtzite ZnO. Presence of $[Zn(C_2O_4).2H_2O]$ was not identified in this sample, which proved the fact that, wurtzite ZnO crystallized at 100 °C. Whereas the MgZnO oxalate precursor contains $[Mg(C_2O_4).2H_2O]$, which was not recognized in samples prepared at a calcination temperature of 400 °C and all peaks were assigned to hexagonal wurtzite structure (see Figure S1A in the Supporting Information). On the other hand, 0.20-MgZnO calcined at 500 °C (Figure 3B) and higher temperatures contains cubic MgO secondary phase, which was identified from the appearance of the (2 0 0) peak (see Figure S1B, C in the Supporting Information). This was consistent with the endothermic DSC peak identified at 460 °C, which represent the crystallization of crystalline MgO from amorphous $Mg(OH)_2$. These results demonstrate the fact that Mg-doped ZnO calcined at 400 °C contains amorphous $Mg(OH)_2$, and at high temperature (above 460 °C) $Mg(OH)_2$ decomposes and leads to Mg^{2+} diffusion into the ZnO lattice structure. All other Mg-doped ZnO samples obtained after calcination in the 400−700 °C temperature range was phase pure. The observed phase transformation with increasing Mg content can be attributed to the fact that when the Mg and Zn atoms bond to the O atom, the Mg atom loses electrons more easily than the Zn atom because of the lower electronegativity of Mg (1.31) in contrast to Zn (1.65). In addition, the large angle between the nearest-neighbor Zn−O bonds than the nearest-neighbor Mg−O bonds leads to stronger interaction between the second nearest-neighbor Mg−O bonds because of the stronger polarity of the Mg−O bonds and hence results in deviation of crystal structure from wurtzite as the quantity of the Mg−O bond is increased.

The crystallite sizes of ZnO samples obtained at various calcination temperatures were highly dependent on the ZnO: Mg ratio (see Figure S2A in the Supporting Information). For example, at a calcination temperature of 400 °C, pure ZnO has a crystallite size of 26 ± 3 nm, whereas a smaller crystallite size of 8 ± 3 nm was observed for 0.20-MgZnO. This reveals the fact that Mg-doping results in the gradual deterioration of ZnO crystallinity, which could be due to lattice disorder and strain induced by Mg^{2+} ions substitution. In addition to this, with an increase in the Mg-content, the (0 0 2) and (1 0 0) XRD peaks slightly shifted toward higher and lower diffraction angles, respectively (see Figure S3 in the Supporting Information). Variation of the lattice parameters and decrease of c/a ratio for samples calcined at 600 °C are presented in Table 1. Similar

Table 1. Lattice Parameters of ZnO Samples Calcined at 600 °C

composition	a (Å)	c (Å)	c/a
ZnO	3.241	5.196	1.603
0.02-MgZnO	3.242	5.196	1.602
0.05-MgZnO	3.247	5.193	1.599
0.10-MgZnO	3.248	5.190	1.597
0.20-MgZnO	3.249	5.185	1.595

lattice parameter changes were also identified for samples calcined at a higher temperature 700 °C (see Table S2 in the Supporting Information). This could be due to structural adjustment as the variation of lattice constant is related to the bond flex of anion and cation, radius difference of substitutional ion, and change of crystal structure. According to Vegard's law, the observed c-axis compression is quite expected for a Mg-substituted ZnO solid solution as the ionic radius of Mg^{2+} (0.57 Å) is smaller than that of Zn^{2+} (0.60 Å).[30,39] The c/a ratio of samples calcined at a low temperature 400 °C remains almost constant (see Table S1 in the Supporting Information), which can be related to the existence of Mg as amorphous $Mg(OH)_2$. The smaller crystallite sizes of Mg-doped ZnO particles were further confirmed by high-resolution scanning electron microscopy (HRSEM). Figure 4 represents the HRSEM micrographs of ZnO and 0.20-MgZnO samples calcined at 600 °C. Uniform particle size distribution of ZnO and 0.20-MgZnO were identified from these images, and ZnO samples possess slightly elongated morphology in comparison to 0.20-MgZnO. Particle sizes of ZnO and 0.20-MgZnO calculated from this micrograph was 62 ± 5 nm and 50 ± 5 nm, respectively, which is in good agreement with the XRD results.

X-ray photoelectron spectroscopic analysis was performed on undoped and Mg-doped ZnO samples in order to investigate the chemical state of Mg, and its effect on the ZnO crystal

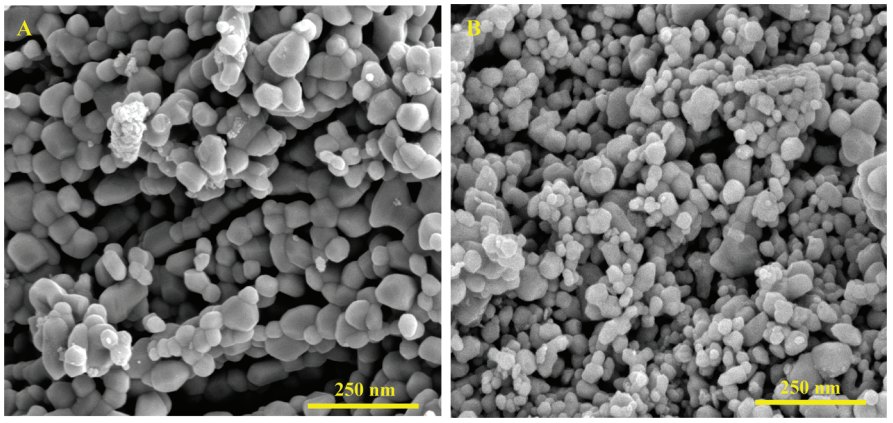

Figure 4. HRSEM micrograph of ZnO samples calcined at 600 °C: (A) ZnO and (B) 0.20-MgZnO.

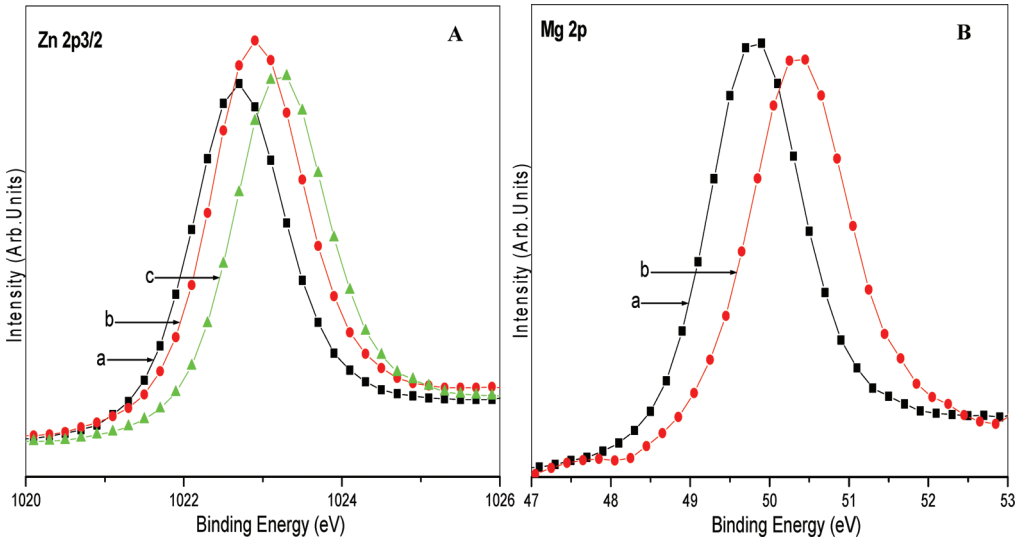

Figure 5. (A) Zn 2p3/2 XPS peaks of ZnO samples calcined at 600 °C: (a) ZnO, (b) 0.05-MgZnO, (c) 0.20-MgZnO; and (B) Mg 2p XPS peaks of ZnO samples calcined at 600 °C: (a) 0.05-MgZnO, (b) 0.20-MgZnO.

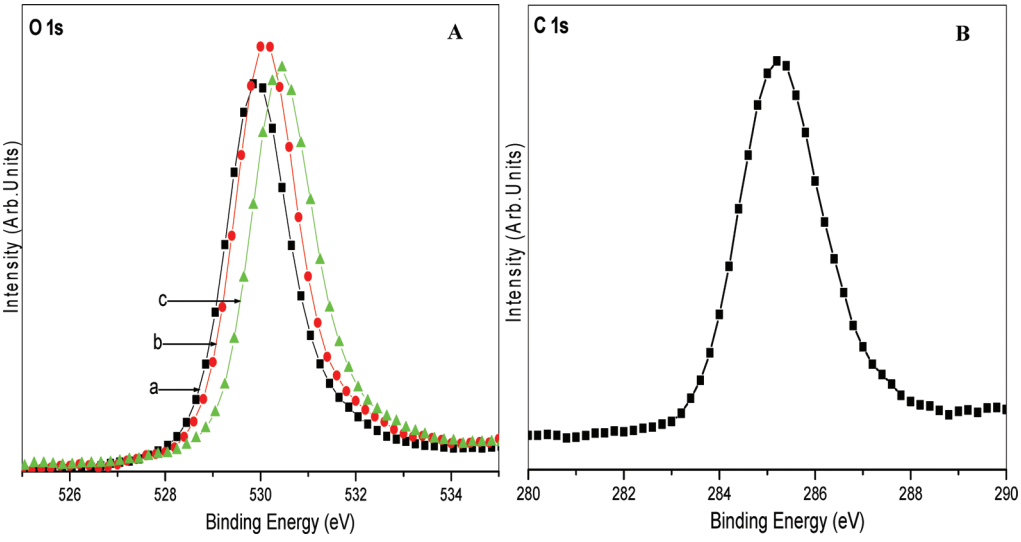

Figure 6. (A) O 1s and (B) C 1s XPS peaks of ZnO samples calcined at 600 °: (a) ZnO, (b) 0.05-MgZnO, (c) 0.20-MgZnO.

structure (Figures 5 and 6). MgZnO has two different crystal structures, hexagonal wurtzite and rock salt cubic. Their presence in the calcined samples depends on the Mg content. The addition of Mg to ZnO can either replace Zn^{2+} or form MgO secondary phase. In the case of undoped ZnO, the Zn 2p3/2 XPS peak appeared at 1022.7 eV represents the

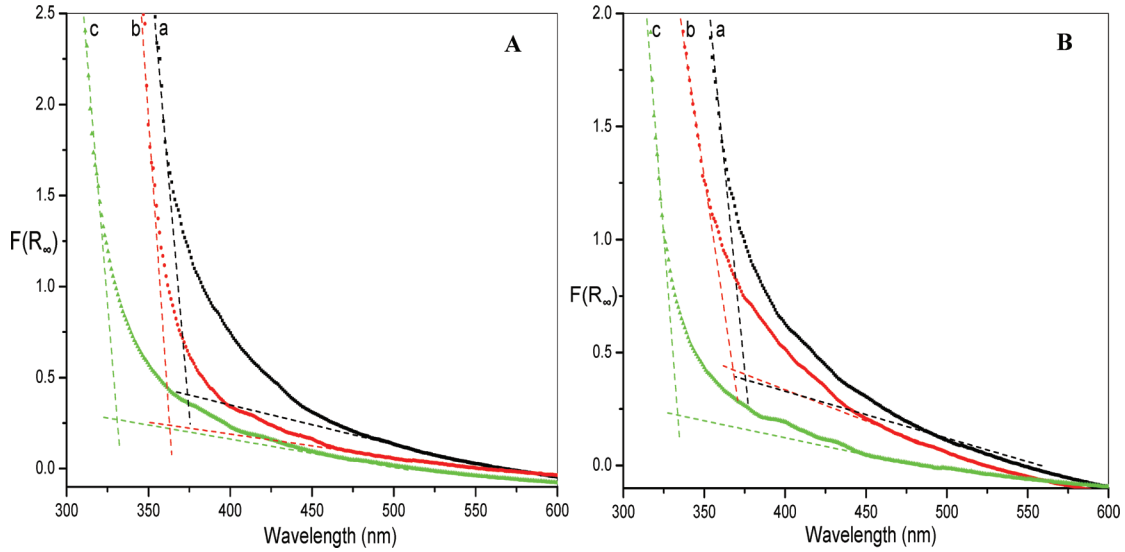

Figure 7. Optical absorption spectra of ZnO samples calcined at (A) 600 °C and (B) 700 °C: (a) ZnO, (b) 0.05-MgZnO, (c) 0.20-MgZnO.

formation of Zn−O bonds (Figure 5A).[21,40] On increasing the Mg content, the Zn 2p3/2 peak shifted to higher binding energies, which results from the replacement of Zn^{2+} by Mg^{2+} and an added Zn−O−Mg binding energy.[40] This Zn−O bond strengthening was in good agreement with the higher FTIR stretching frequency of Zn−O bonds of ZMO samples in contrast to undoped ZnO. The Mg 2p XPS peak centered at 49.8 eV for 0.05-MgZnO can be ascribed to the presence of Mg^{2+} replacing Zn^{2+} (Figure 5B).[41] The positive Mg 2p binding energy shift toward the Mg 2p (MgO) binding energy of 50.80 was identified for 0.2-MgZnO, which was in correlation with the crystallization of cubic MgO secondary phase in 0.2-MgZnO. These results are consistent with the Mg 2p XPS peaks obtained in other studies.[42,43] The O 1s peak at 529.6 eV corresponds to O^{2-} ions on the wurtzite structure of the Zn^{2+} ion array, surrounded by Zn (Figure 6A).[21,44] Higher O 1s binding energies identified on increasing the Mg-content can be ascribed to the added contribution from Zn−O−Mg (530.2 eV) and Mg−O (530.8 eV) bonds.[21,45] The presence of adventitious elemental carbon in all samples (Figure 6B), which is an unavoidable presence on all air-exposed materials, were also identified from the C 1s peak at 285 eV.[46]

The UV−vis absorption spectra of ZnO and MgZnO samples obtained after calcination at 600 and 700 °C are presented in Figure 7. With an increase in Mg-content, the absorption edge of ZnO clearly shifts to the blue region, which results in the band gap widening. For example, at a calcination temperature of 600 °C, undoped ZnO has a band gap value of 3.32 eV, whereas 0.20-MgZnO has a wider band gap of 3.75 eV (Table 3). The increase of optical band gap energy with Mg-doping can be attributed to the so-called Moss-Burstein effect caused by electrons generated by oxygen vacancies.[47,48] Substitution of Zn^{2+} by Mg^{2+} results in an increase in oxygen vacancies and electron concentration due to the electronegativity and ionic radius difference between Zn and Mg. This increase in carrier density results in the lifting of the Fermi-level into the conduction band of the degenerate semiconductor and a consequent band gap widening. Band gap increase with increase in Mg-content can be explained by the generation of more oxygen vacancies and electrons. The band gap widening due to the Moss−Burstein effect was also observed for other

Table 2. Textural Properties of ZnO Samples Calcined at 400 and 600 °C

composition	surface area (m^2/g)	pore diameter (nm)	pore volume (cc/g)
ZnO-400 °C	35.66	20.73	0.291
0.02-MgZnO-400 °C	39.21	20.69	0.320
0.10-MgZnO-400 °C	54.48	12.22	0.336
0.20-MgZnO-400 °C	71.86	11.96	0.353
ZnO-600 °C	4.29	4.58	0.025
0.02-MgZnO-600 °C	6.98	4.62	0.079
0.10-MgZnO-600 °C	12.52	12.32	0.091
0.20-MgZnO-600 °C	17.36	20.44	0.137

Table 3. Band Gap Values of ZnO Samples Calcined at Various Temperatures

	band gap (eV)		
composition	400 °C	600 °C	700 °C
ZnO	3.34	3.32	3.30
0.02-MgZnO	3.35	3.36	3.32
0.05-MgZnO	3.37	3.41	3.37
0.10-MgZnO	3.37	3.48	3.45
0.20-MgZnO	3.38	3.75	3.71

semiconductors such as Al-doped ZnO, Sn-doped In_2O_3, and Cd-doped In_2O_4.[47,49,50] Lattice parameter is another important factor affecting the band gap of semiconductors, and increase in band gap values were observed with a decrease of c/a ratio.[51−53] As discussed previously, due to the differences in the electronegativities and ionic radius, substitution of Zn^{2+} (0.60 Å) by Mg^{2+} (0.57 Å) results in the c-axis compression and a consequent band gap widening. Very low band gap widening observed for MgZnO samples obtained at 400 °C can be attributed to the existence of Mg as amorphous $Mg(OH)_2$ in Mg-doped ZnO samples. Thus MgZnO could be considered not only as an ultraviolet light emitting material, but also as

ultraviolet absorption material, whose absorption energy can be adjusted by varying the Mg content.

Nitrogen adsorption isotherms of undoped and Mg-doped ZnO samples showed type IV characteristics with H1 type (cylindrical shape) of hysteresis (Figure 8).[54] With an increase

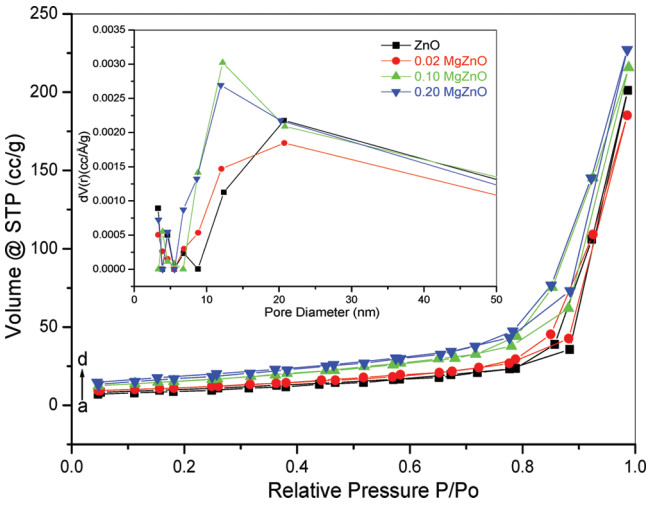

Figure 8. N_2 adsorption–desorption isotherm and the pore size distribution (inset) of ZnO samples calcined at 400 °C: (a) ZnO, (b) 0.02-MgZnO, (c) 0.10-MgZnO, (d) 0.20-MgZnO.

in Mg- content, the steepness of the hysteresis loop increased and the end of the hysteresis loop shifted toward lower relative pressure (P/P_0), which represents their superior textural properties. For example, ZnO containing highest amount of dopant 0.20-MgZnO calcined at 400 °C has a 2-fold increases in surface area (Table 2). In addition to this, Mg-doped ZnO samples possess lower pore diameters and higher pore volume in contrast to the pure ZnO calcined at same temperature. Both ZnO- and Mg-doped ZnO samples showed a considerable decrease in surface area and pore volume with an increase in calcination temperature. Smaller crystallite size and increased Zn–O bond strength of Mg-doped ZnO nanoparticles may be the critical factors responsible for their superior textural properties at all calcination temperatures. Thus it is evident from the above observations that the oxalate coprecipitation method results in the formation of nanostructured MgZnO possessing wide band gap and superior textural properties in contrast to undoped ZnO.

3.2. Sunlight-Induced Photocatalytic Activity of Mg-Doped ZnO. Mg-doped ZnO obtained at various calcination temperatures exhibited enhanced sunlight-induced photocatalytic decomposition of methylene blue in comparison to the undoped ZnO. At all calcination temperatures, the photocatalytic activities were found to be a function of the Mg-concentration (see Table S3 in the Supporting Information). On increasing the Mg-content, photocatalytic activities increased and 0.10-MgZnO exhibited highest activity. Whereas, further increase in the Mg-content caused a drastic reduction in the photocatalytic activity, and 0.20-MgZnO obtained at all calcination temperatures showed the lowest activity. The most photoactive sample 0.10-MgZnO obtained at 600 °C showed 2-fold higher photocatalytic activity in contrast to undoped ZnO (Figure 9A & 9B). The calculated rate constants for undoped ZnO, 0.10-MgZnO, and 0.20-MgZnO calcined at 600 °C were 0.3167, 0.6300, and 0.1577 min^{-1}, respectively (Figure 9C). On increasing the calcination temperature above 600 °C, both undoped and Mg-doped ZnO samples exhibited reduced photocatalytic activities.

Significantly higher sunlight-induced photocatalytic activities of Mg-doped ZnO can be explained by their increased band gap values and superior textural properties. It is clear from the XRD, FT-IR, XPS, BET, and UV–vis spectroscopy results that the Mg-doping of ZnO results in the formation of wide band gap nanocrystalline $Zn_{1-x}Mg_xO$ photocatalysts possessing improved textural properties. An increase in the band gap values causes higher redox potential of the photoexcited electron–hole pairs, which significantly increases the activity of the photocatalyst. Considering the fact that photocatalytic reactions mainly occur on the catalyst surface, increasing the surface area was one of the previously employed methods to increase the photocatalytic reaction rate.[4,5] In the case of Mg-doped ZnO, both band gap and textural properties increases with an increase of Mg content. As a result, a 2-fold increase in the sunlight induced photocatalytic activity of 0.10-MgZnO calcined at 600 °C can be attributed to its superior textural properties and wide band gap. Though 0.20-MgZnO prepared at all calcination temperatures possesses the best textural properties and the widest band gap, the photocatalytic activity of this sample was less that that of undoped ZnO. This point toward the fact that textural properties and band gap are not the only factors controlling the sunlight induced photocatalytic activity of Mg-doped ZnO. Poor textural properties due to excessive grain growth may be the critical factor responsible for the reduced photocatalytic activities of Mg-doped ZnO samples prepared above 600 °C.

Photoluminescence (PL) spectroscopy was employed for further investigation of the photocatalytic activities of Mg-doped ZnO. Photoluminescence spectra of undoped ZnO, the most active photocatalyst 0.10-MgZnO and the least active sample 0.20-MgZnO obtained at 600 °C are presented in Figure 9D. Because the PL emission results from the recombination of photoinduced charge carriers, information regarding the presence of surface states, efficiency of charge carrier trapping and their recombination kinetics can be drawn from the PL spectra.[55] This technique has been widely used in order to understand the fate of electron–hole pairs in semiconductor particles, and a strong correlation between PL intensity and photocatalytic activity has been previously reported.[4,5,55] Reduced near band edge (NBE) and excitonic emission intensities were identified for the most active photocatalyst 0.10-MgZnO in contrast to undoped ZnO. This can be attributed to the efficient separation of photoinduced charge carriers due to the band gap widening resulting from the replacement of Zn^{2+} by Mg^{2+}. On the other hand, intensities of these peaks were much higher in the case of the least active photocatalyst 0.20-MgZnO, which represent faster recombination of photoinduced electron–hole pairs. This may be due to the crystallization of cubic MgO secondary phase, which may act as electron–hole recombination centers. In addition to this, with an increase of Mg-content, the NBE emission peak of MgZnO exhibited a blue shift, which is in good agreement with their increased band gap values identified from UV/vis spectroscopy.

The significant differences in the PL intensities confirmed a considerable change in the electronic structure of ZnO with an increase in Mg-content, which was in agreement with the binding energy changes of constituent atoms identified from XPS studies. Lower NBE and excitonic PL intensities resulting

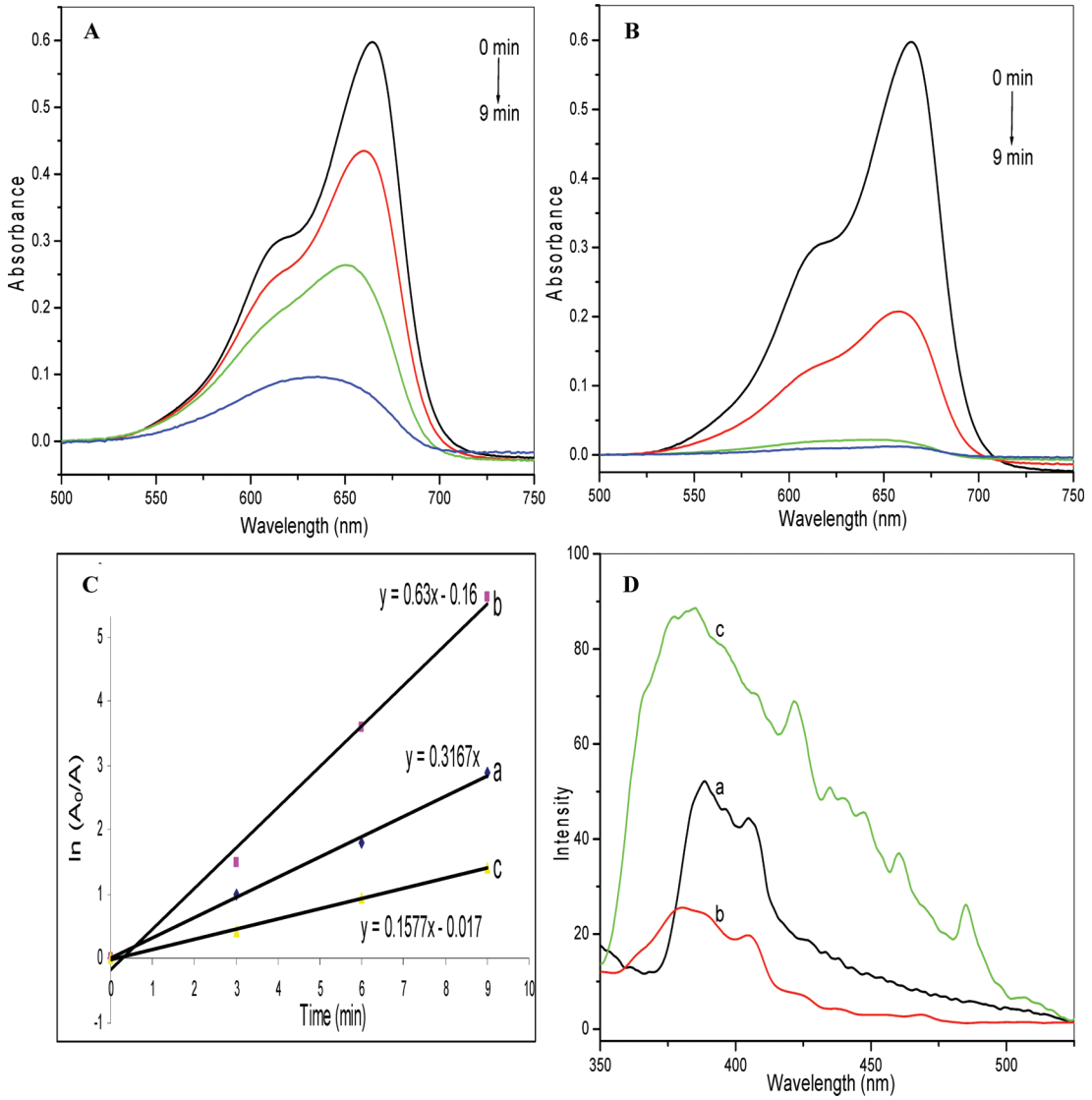

Figure 9. (A) Absorption spectra of sunlight induced methylene blue degradation using ZnO calcined at 600 °C and (B) using 0.10-MgZnO calcined at 600 °C. (C) Kinetic study of photocatalytic methylene blue degradation using (a) ZnO calcined at 600 °C, (b) 0.10-MgZnO calcined at 600 °C, and (c) 0.20-MgZnO calcined at 600 °C. (D) Photoluminescence spectra of ZnO samples calcined at 600 °C: (a) ZnO, (b) 0.10-MgZnO, (c) 0.20-MgZnO.

from efficient charge separation were reported for ZnO and TiO_2 doped with Sn, W, Ag, and Au.[56−60] These semiconductors showing lower PL intensities were also reported to exhibit superior photocatalytic activities. In short, any factor that can promote efficient electron−hole separation can lower both the NBE and the excitonic PL intensities and cause an increase in the photocatalytic activity. These facts and the lowest PL intensity of 0.10-MgZnO point toward the fact that efficient charge separation is another critical factor responsible for its enhanced sunlight induced photocatalytic activity. Thus it can be concluded that increased band gap values, superior textural properties and efficient electron−hole separation are the factors responsible for the enhanced sunlight-driven photocatalytic activities of Mg-doped ZnO.

4. CONCLUSIONS

Magnesium-doped ZnO (ZMO) nanoparticles were synthesized through an oxalate coprecipitation method. After calcination at temperatures ranging from 400 to 700 °C, ZMO compositions containing lower Mg-content exists as pure wurtzite phase, whereas, crystallization of cubic MgO secondary phase was identified for 0.2-MgZnO. All ZMO particles exhibited smaller crystallite size, reduced c/a ratio, enhanced textural properties and wider band gap in contrast to undoped ZnO. The presence of Mg as Mg^{2+} ions and MgO secondary phase, which results in the strengthening of Zn−O bonds was identified from the XPS analysis. In addition to this, XPS studies demonstrated significant changes in the electronic structure ZnO as a result of Mg-doping. Wurtzite phase ZMO samples exhibited a blue-shift in the near band edge photoluminescence (PL) emission, reduced PL intensities, and enhanced sunlight-induced photocatalytic activities compared to undoped ZnO, whereas the ZMO composition 0.2-MgZnO containing MgO secondary phase showed the highest PL intensity and lowest photocatalytic activity. The most active sample 0.1-MgZnO obtained at 600 °C showed a 2-fold enhancement in the sunlight-induced photocatalytic decomposition of methylene blue. The highest photocatalytic activity

of 0.1-MgZnO calcined at 600 °C was due to the combined effect of better electron−hole separation, a wider band gap, and superior textural properties compared to the undoped ZnO. The studies described herein demonstrate that Mg-doped ZnO nanoparticles can be utilized for efficient sunlight-driven photocatalytic, self-cleaning, and photovoltaic applications.

■ ASSOCIATED CONTENT

Supporting Information

X-ray diffraction pattern of ZnO samples calcined at 400, 600, and 700 °C. Crystallite size and variation of ZnO samples calcined at 400−700 °C. Variation in lattice parameters of ZnO samples calcined at 400, 600, and 700 °C. Photocatalytic rate constants of ZnO samples calcined at various temperatures. This material is available free of charge via the Internet at http://pubs.acs.org/.

■ AUTHOR INFORMATION

Corresponding Author

*E-mail: vkumar10@yahoo.com.

Notes

The authors declare no competing financial interest.

■ REFERENCES

(1) O'Regan, B.; Grätzel, M. *Nature* **1991**, *353*, 737.
(2) Kamat, P. V. *J. Phys. Chem. C* **2007**, *111*, 2834.
(3) Mills, A.; Lee, S. K. *J. Photochem. Photobiol., A* **2002**, *152*, 233.
(4) Etacheri, V.; Seery, M. K.; Hinder, S. J.; Pillai, S. C. *Adv. Funct. Mater.* **2011**, *21*, 3744.
(5) Etacheri, V.; Seery, M. K.; Hinder, S. J.; Pillai, S. C. *Chem. Mater.* **2010**, *22*, 3843.
(6) Anie, R.; Joseph, C.; Ittyachen, M. A. *Mater. Lett.* **2001**, *49*, 299.
(7) Afzaal, M.; Malik, M. A.; O'Brien, P. *New J. Chem.* **2007**, *31*, 2029.
(8) Vayssieres, L. *Adv. Mater.* **2003**, *15*, 464.
(9) Wang, Z. L. *ACS Nano* **2008**, *2*, 1987.
(10) Kılınç, N.; Arda, L.; Öztürk, S.; Öztürk, Z. Z. *Cryst. Res. Technol.* **2010**, *45*, 529.
(11) Gouvea, C. A. K.; Wypych, F.; Moraes, S. G.; Duran, N.; Nagata, N.; Zamora, P. P. *Chemosphere* **2000**, *40*, 433.
(12) Kansal, S. K.; Singh, M.; Sud, D. *J. Hazard. Mater.* **2007**, *141*, 581.
(13) Muruganandham, M.; Chen, I. S.; Wu, J. J. *J. Hazard. Mater.* **2009**, *172*, 700.
(14) Sakthivel, S.; Neppolian, B.; Shankar, M. V.; Arabindoo, B.; Palanichamy, M.; Murugesan, V. *Sol. Energy Mater. Sol. Cells* **2003**, *77*, 65.
(15) Chakrabarti, S.; Dutta, B. K. *J. Hazard. Mater.* **2004**, *112*, 269.
(16) Lu, X.; Liu, Z.; Zhu, Y.; Jiang, L. *Mater. Res. Bull.* **2011**, *46*, 1638.
(17) Li, G. R.; Bu, Q.; Zheng, F. L.; Su, C. Y.; Tong, Y. X. *Cryst. Growth Des.* **2009**, *9*, 1538.
(18) Luo, T.; Yang, Y. C.; Zhu, X. Y.; Chen, G.; Zeng, F.; Pan, F. *Phys. Rev. B* **2010**, *82*, 14116.
(19) Wang, H. B.; Wang, H.; Zhang, C.; Yang, F. J.; Duan, J. X.; Yang, C. P.; Gu, H. S.; Zhou, M. J.; Li, Q.; Jiang, Y. *J. Nanosci. Nanotechnol.* **2009**, *5*, 3308.
(20) Quintana, M.; Edvinsson, T.; Hagfeldt, A.; Boschloo, G. *J. Phys. Chem. C* **2007**, *111*, 1035.
(21) Hullavarad, S. S.; Hullavarad, N. V.; Pugel, D. E.; Dhar, S.; Venkatesan, T.; Vispute, R. D. *Opt. Mater.* **2008**, *30*, 993.
(22) Yadav, M. K.; Ghosh, M.; Biswas, R.; Raychaudhuri, A. K.; Mookerjee, A. *Phys. Rev. B* **2007**, *76*, 195450.
(23) Boshta, M.; Abou-Helal, M. O.; Ghoneim, D.; Mohsen, N. A.; Zaghlool, R. A. *Surf. Coat. Technol.* **2010**, *205*, 271.
(24) Kwon, Y.; Li, Y.; Heo, Y. W.; Jones, M.; Holloway, P. H.; Norton, D. P.; Park, Z. V.; Li, S. *Appl. Phys. Lett.* **2004**, *84*, 2685.
(25) Masuda, S.; Kitamura, K.; Okumura, Y.; Miyatake, S.; Tabata, H.; Kawai, T. *J. Appl. Phys.* **2003**, *93*, 1624.
(26) Rao, B. B. *Mater. Chem. Phys.* **2000**, *64*, 62.
(27) Birkmire, R. W.; Eser, E. *Annu. Rev. Mater. Sci.* **1997**, *27*, 625.
(28) Aoki, T.; Hatanaka, Y.; Look, D. C. *Appl. Phys. Lett.* **2000**, *76*, 3257.
(29) Chopra, K. L.; Major, S.; Pandya, D. K. *Thin Solid Films* **1983**, *102*, 1.
(30) Kaushal, A.; Kaur, D. *Sol. Energy Mater. Sol. Cells* **2009**, *93*, 193.
(31) Ning, G. H.; Zhao, X. P.; Li, J. *Opt. Mater.* **2004**, *27*, 1.
(32) Ma, Z. Q.; Zhao, W. G.; Wang, Y. *Thin Solid Films* **2007**, *515*, 8611.
(33) Zhuang, L.; Wong, K. H. *Thin Solid Films* **2008**, *516*, 5607.
(34) West, A. R. *Solid State Chemistry and Its Applications*; John Wiley & Sons: London, 1984.
(35) Shan, F. K.; Kim, B. I.; Liu, G. X.; Liu, Z. F.; Sohn, J. Y.; Lee, W. J.; Shin, B. C.; Yu, Y. S. *J. Appl. Phys.* **2004**, *95*, 4772.
(36) Pillai, S. C.; Kelly, J. M.; McCormack, D. E.; O'Brien, P.; Ramesh, R. *J. Mater. Chem.* **2003**, *13*, 2586.
(37) Jimenez-Gonzalez, A. E.; S. U., J. A.; Suarez-Parra, R. *J. Cryst. Growth* **1998**, *192*, 430.
(38) Mohandes, F.; Davar, F.; Salavati-Niasari, M. *J. Phys. Chem. Solids* **2010**, *71*, 1623.
(39) Shannon, R. D. *Acta Crystallogr., Sect. A* **1976**, *32*, 751.
(40) Jing, L.; Xu, Z.; Shang, J.; Sun, X.; Cai, W.; Guo, H. *Mater. Sci. Eng., A* **2002**, *332*, 356.
(41) Gangil, S.; Nakamura, A.; Yamamoto, K.; Ohashi, T.; Temmyo, J. *J. Korean Phys. Soc.* **2008**, *53*, 212.
(42) Wei, Z. P.; Yao, B.; Zhang, Z. Z.; Lu, Y. M.; Shen, D. Z.; Li, B. H.; Wang, X. H.; Zhang, J. Y.; Zhao, D. X.; Fan, X. W.; Tang, Z. K. *Appl. Phys. Lett.* **2006**, *89*, 1021104.
(43) Lee, C. Y.; Tseng, T. Y.; Li, S. Y.; Lin, P. *J. Appl. Phys.* **2006**, *99*, 24303.
(44) Langer, D. W.; Vesely, C. J. *Phys. Rev. B* **1970**, *2*, 4885.
(45) Nefeddov, V. I.; Firsov, M. N.; Shaplygin, I. S. *J. Electron Spectrosc. Relat. Phenom.* **1982**, *26*, 625.
(46) Sakthivel, S.; Kisch, H. *Angew. Chem., Int. Ed.* **2003**, *42*, 4908.
(47) Sernelius, B. E.; Berggren, K. F.; Jin, Z. C.; Hamberg, I.; Granqvist, C. G. *Phys. Rev. B* **1988**, *37*, 10244.
(48) Li, Z.; Shen, W.; Xue, S.; Zu, X. *Colloids Surf., A* **2008**, *320*, 156.
(49) Vink, T. J.; Overwijk, M. H. F.; Walrave, W. *J. Appl. Phys.* **1996**, *80*, 3734.
(50) Wang, W. L.; Gao, J. Y.; Lao, K. J.; Peng, D. L.; Jiang, S. R. *Mater. Lett.* **1992**, *13*, 342.
(51) Machlin, E. S. *Materials Science in Microelectronics: The Effects of Structure on Properties in Thin Films*; Elsevier: Amsterdam, 2006.
(52) Wunderlich, W.; Miao, L.; Tanemura, M.; Tanemura, S.; Jin, P.; Kaneko, K.; Terai, A.; Nabatova-Gabin, N.; Belkada, R. *Int. J. Nanosci.* **2004**, *3*, 439.
(53) Na-Phattalung, S.; Smith, M. F.; Kim, K.; Du, M.-H.; Wei, S.-H.; Zhang, S. B.; Limpijumnong, S. *Phys. Rev. B: Condens. Matter* **2006**, *73*, 125205.
(54) Nasar, R. S.; Cerqueira, M.; Longo, E.; Varela, J. A. *Cerâmica.* **2008**, *54*, 38.
(55) Liqiang, J.; Yichun, Q.; Baiqi, W.; Shudan, L.; Baojiang, J.; Libin, Y.; Wei, F.; Honggang, F.; Jiazhong, S. *Sol. Energy Mater. Sol. Cells* **2006**, *90*, 1773.
(56) Shang, J.; Yao, W. Q.; Zhu, Y. F.; Wu, N. *Appl. Catal., A* **2004**, *25*, 257.
(57) Jing, L. Q.; Fu, H. G.; Wang, D. J.; Wei, X.; Sun, J. Z. *Acta Phys. Chim. Sin.* **2005**, *21*, 38.
(58) Li, X. Z.; Li, F. B.; Yang, C. L.; Ge, W. K. *J. Photochem. Photobiol. A* **2001**, *141*, 209.
(59) Xin, B. F.; Jing, L. Q.; Ren, Z. Y.; Wang, B. Q.; Fu, H. G. *J. Phys. Chem. B* **2005**, *109*, 2805.
(60) Li, F. B.; Li, X. Z. *Appl. Catal., A* **2002**, *228*, 15.